Engineering Analysis with Boundary Elements 77 (2017) 145–156

Contents lists available at ScienceDirect

Engineering Analysis with Boundary Elements

journal homepage: www.elsevier.com/locate/enganabound

Freeze-drying modeling of vial using BEM

M. Ramšak, J. Ravnik, M. Zadravec, M. Hriberšek, J. Iljaž*

Faculty of Mechanical Engineering, University of Maribor, Smetanova 17, SI-2000 Maribor, Slovenia

ARTICLE INFO

Keywords:
Freeze-drying
Vial
Heat and mass transfer
Subdomain boundary element method
Sublimation

ABSTRACT

The paper reports on development of Boundary Element Method (BEM) based numerical algorithm for the numerical simulation of the freeze drying process in a vial. In the paper the problems of freeze-drying modeling are covered in detail. The BEM based algorithm is developed for the axisymmetrical geometry case using the Subdomain BEM approach. A special feature of the algorithm is an implicit representation of the interface conditions at the sublimation front, which is a great advantage of the proposed numerical scheme. As a test case the freeze drying of skim milk in a vial is selected. The numerical results show a good agreement with reference data proving that the developed numerical model is appropriate, accurate and fast in simulating the primary and secondary drying stage. The numerical analysis also shows that the time step during the secondary drying stage can be increased by a factor 100, which reduces the computational time drastically.

1. Introduction

Freeze-drying or lyophilization is a process of removing the liquid phase, usually water, from the initial wet compound or solution and can be divided into three stages. The first stage is freezing of the base compound to solidify it, then the surrounding pressure is lowered to the level where the frozen water can sublimate and the second stage begins represented by the sublimation process of the frozen water (primary drying). After the sublimation process ends the third stage begins that is described by the desorption of the bounded water in the dried material (secondary drying). Because the freeze-drying process is controlled at relatively low temperatures, the base material is preserved with all its quality and also becomes more stable [1]. For this reason, the freeze-drying process is mostly used in the food, chemical, pharmaceutical and biotechnological industry [2–4,1]. In the food industry the product is usually placed freely on the trays, where in the pharmaceutical industry the product (solution) is predominantly filled in vials.

The freeze-drying is due to the slow drying rate and high investment cost into the equipment and product batch, a very expensive process. Therefore it needs a careful process planning and control, with the aim to reduce the drying time and to be as energy efficient as possible [2,5–7,4,8–10]. To be able to predict the correct drying times and to set the correct process control so the temperature of the frozen solution or material does not exceed the melting or scorch temperature during the drying process, a good mathematical or numerical model is needed.

Numerical modeling of freeze-drying process is very demanding because of the needed knowledge of the heat and mass transfer including the phase change of liquid (water). The general numerical model can be used to describe the freeze-drying process in many systems, like vials that are very popular in the pharmaceutical industry. However, the freeze-drying process has many characteristics that had to be included into the numerical model for successful simulation. The first characteristic is that the freeze-drying process is a time dependent problem, because of the moving sublimation front and changing parameter values of the process. The heat and mass transfer is governed by the conservation laws of mass, momentum and energy. The sublimation process at the moving sublimation interface between the frozen and dried region has to be included as well as the desorption of the bounded water in the dried region. The second characteristic is that the ratio of heat transfer by conduction, convection and radiation at freeze-drying in vials is very different from the ratio of drying process at the atmospheric conditions, because of the much lower surrounding pressure, which almost eliminates the convection. Therefore, the conduction and the radiation plays a major role in the heat transfer process [7,5,2]. The next characteristic is that the dried material is highly porous, which can not be described directly due to the complex internal structure. Therefore, the dry material had to be modeled using the porous model approach. The freeze-drying process and also the mass transfer of the liquid phase take place at very low static pressure, where the free range between the molecules is very large and consequently also the Knudsen number, which questions the correctness of using the governing equations that are written for the

* Corresponding author.
E-mail address: jurij.iljaz@um.si (J. Iljaž).

http://dx.doi.org/10.1016/j.enganabound.2017.01.011
Received 16 November 2016; Received in revised form 26 January 2017; Accepted 30 January 2017

continuum phase. This is especially problematic for modeling of the momentum transfer and condensation of the liquid phase (water) in the lyophilizator chamber and condenser [11,12].

For these reasons, the numerical modeling of freeze-drying process in general is a very demanding task to do, and the accuracy of computational models depend on the used mathematical model. However, to be able to simulate freeze-drying process in the whole lyophilizator, we first need to successfully model and solve the problem of product freeze-drying, what is the main focus of the reported work here. Through the years, several different mathematical models describing heat and mass transfer in the freeze-drying process have been proposed. From the most simple ones [5] to the advanced models using partial differential equations (PDE) [13–15]. The "sorption-sublimation" model described in [14–18] has proven to be accurate and successful in simulating the freeze-drying process in vial solution. Mascarenhas et al. [17] solved the freeze-drying model using Finite Element Method (FEM) with arbitrary Lagrangian-Eulerian (ALE) scheme. They applied the 2D axisymmetrical model to the freeze-drying problem in a vial for protein Bovine Somatotropin (BST) and skim milk, where the latter problem has been treated as a 1D problem. Sheehan and Liapis [2] upgraded the problem description with more accurate boundary conditions where they included the radiation and solved the model using the Finite Difference method (FDM). They applied their numerical model to the freeze-drying of skim milk in vials and investigated three different cases, by changing vial at different locations (center or corner) and setting different process controls for not exceeding the melting and scorch temperature. Recently Song et al. [19,18] and Nam and Song [20] used the Finite Volume Method (FVM) to solve the mathematical model described by Sheehan and Liapis [2] to solve problem of skim milk freeze-drying in vial. Since Boundary Element Method solves the integral representation of the governing equations by using special weighting functions and simultaneously solve the resulting system of equations for the function and its derivative, this paper reports on the novel implementation of the Boundary Element Method (BEM) for the numerical solution of the "sorption-sublimation" model of freeze-drying in vial.

As stated, the paper is focused on the development of numerical model for freeze-drying simulation of skim milk in one vial using BEM to solve the complex system of non-linear governing equations in space and time domain. The used BEM approach has been already successfully implemented to various numerical problems from fluid dynamics [21–24], moisture transport [25], bioheat problems [26,27], as well as the solid-liquid phase change problems [28–30].

The paper is organized as follows. Section 2 describes the freeze-drying in a vial in more detail especially the heat and mass transfer phenomena. The derived governing equations (mathematical model) with the description are reported in Section 3. The Section 4 covers the description of the implemented BEM with fundamental solution and numerical discretization of governing equations, yielding the complete numerical model for freeze-drying simulation in vials. Computational example with validation, results and discussion is presented in Section 5. The paper ends with the conclusion and acknowledgment in Section 6 and 7, respectively.

2. Freeze-drying in a vial

The case under consideration is the freeze-drying stage in vial, which is typically placed on the tray inside a lyophilizator drying chamber. The vial which contains a drying substance is schematically shown on Fig. 1, where three main areas can be observed:

- the area above the initial free surface of the drying substance, consisting of vacuum and evaporated solvent (water vapor),
- the porous region above the sublimation interface, consisting of solid matrix with adsorbed solvent,

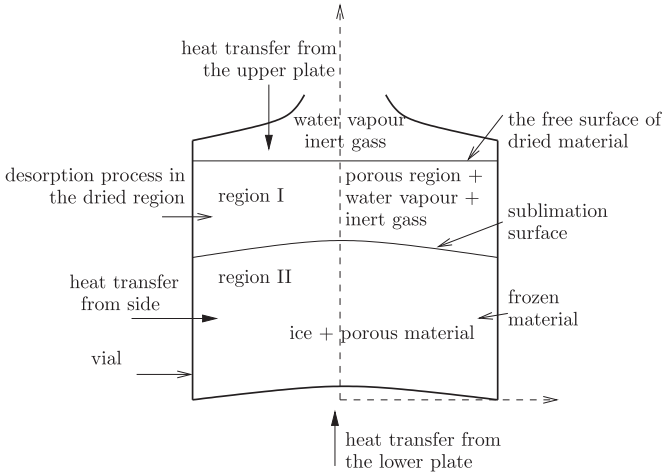

Fig. 1. Basic data on freeze drying in a vial.

- the porous region below the sublimation interface, consisting of frozen solvent and solid matrix with adsorbed solvent.

The process starts when the frozen substance is subjected to a sudden decrease in pressure, setting the thermodynamic conditions below the triple point of the water for sublimation to occur. The freeze-drying process proceeds as follows. The vial is heated by the two heating plates, one above and one below the vial. The heat is transferred to the frozen substance from the top, the bottom and through the sides of the vial, as shown in Fig. 1. At the top, the heat transfer is mainly due to the radiation, as the vial is not in the direct contact with the upper plate and the low static pressure of the surrounding decreases conduction and convection heat transfer in the vacuum. The heat from below comes from heat radiation and conduction, because of the direct contact between the vial and the lower heating plate. The effect of the heat radiation to the side surface of the vial in general depends on the number and position of the surrounding vials [8], but is frequently neglected, especially in the case of fully packed tray in a standard lyophilizator. Here we can conclude that the main contribution of the vial heating comes from above and below. For these reasons, also many other authors neglect the side heat flux and treat the problem as one-dimensional [5,13,16,17].

The pressure difference between the sublimation surface and the vacuum induces sublimation, which is due to the sublimation enthaply a very energy demanding process. Heating of the shelves solves the problem of energy supply and enables to take control of the process. Because of the opened top of the vial, the drying starts at the top and proceeds toward the bottom of the vial. On the sublimation front or interface, which separates the frozen and already dried region, we assume that the concentration or partial pressure of the water is equal to the equilibrium concentration at the interface temperature, and that the mass flux of the inert gas is equal to zero, which means that the gradient of partial pressure of the inert gas is also equal to zero. In addition, we predict that the temperature on the sublimation front is continuous, while the gradient of the temperature is not, because of the sublimation process, as well as of different thermal conductivity of both regions. The energy conservation law on the interface is described in detail by the used model presented in the next section, here we would like to state only that the net heat flux at the interface also depends on the movement or velocity of the interface. As stated before, the dried region is highly porous, therefore, we can presume that there is no closed pockets and that the inert gas and water vapor can move freely. The movement of gaseous phase in the porous material can be described by the Darcy law. While the sublimation takes place at the interface, the desorption process from the remaining porous solid is also present in the dried region. When all the frozen water is removed

only the desorption remains active to remove the bounded moisture to the desired level.

The freeze-drying process is usually divided into two parts, the primary and secondary drying stage [5,17]. The first stage is represented mainly by the sublimation process of the frozen liquid and it ends when all the frozen water is removed. The desorption process is also present in the primary drying stage in the dried region, but it is not a dominant process. After the first stage, the second stage begins, where the desorption dictates the drying process. This paper covers the modeling of the primary and the secondary drying stage, with the aim to determine or evaluate the overall drying time to achieve the desired level of dryness, which is one of the main goals in the optimization of lyophilization [7,4,10].

3. Governing equations

Freeze-drying process is governed by the mass and energy conservation equations including the moving interface conditions, as described. The energy conservation equation is written for the temperature field in the dried and frozen region while the mass conservation is usually written for the sublimating water in the form of bounded concentration and partial pressure of liquid vapor, and for the inert gas in the form of partial pressure inside the dried region. Therefore, the aim is to obtain the temperature and concentration field of bounded water inside the substance in vial, together with the partial pressure of inert gas and moisture vapor. In the next subsections a more detailed description of the used governing equations is written.

3.1. Conservation of energy

Conservation of energy for the dried region (I) can be stated in the following form:

$$\rho_{e,I}c_{pe,I}\frac{\partial T}{\partial t} + \vec{\nabla}\cdot((\overrightarrow{N_v} + \overrightarrow{N_i})c_{p,g}T) = \vec{\nabla}\cdot(\lambda_{e,I}\vec{\nabla}T) + dH_v\rho_{I,p}\frac{\partial C}{\partial t}, \tag{1}$$

where $\rho_{e,I}$, $c_{pe,I}$ and $\lambda_{e,I}$ represent the effective density, effective specific heat and effective thermal conductivity of the dried region, respectively. T stands for the temperature, C is the bounded water concentration, $\overrightarrow{N_v}$ and $\overrightarrow{N_i}$ represent the mass flux of water vapor and inert gas, respectively, $c_{p,g}$ is the specific heat of the gaseous phase, dH_v the vaporization heat of the bounded liquid and $\rho_{I,p}$ the density of the porous material in the dried region. The first term on the left hand side of Eq. (1) represents the accumulation of the heat, the second one the convection, the third one diffusion and the last one the heat sink due to the desorption process. The time derivative of the bounded water concentration is negative, due to the decreasing concentration, therefore the last term represents the heat sink.

In the frozen region (II) the heat transfer is only governed by the conduction, therefore the heat transfer equation can be written in the following form:

$$\rho_{II}c_{p,II}\frac{\partial T}{\partial t} = \vec{\nabla}\cdot(\lambda_{II}\vec{\nabla}T) = \lambda_{II}\Delta T, \tag{2}$$

where ρ_{II}, $c_{p,II}$ and λ_{II} represent density, specific heat capacity and thermal conductivity of the frozen region, respectively. The term on the left hand side represents the heat accumulation and the term on the right hand side the heat diffusion, which can be expressed by Laplace in the case of constant heat conductivity. For the frozen material it is assumed to be homogeneous and to have constant material properties ($\lambda_{II} = const.$), therefore the diffusion is described with the Laplace function.

3.2. Conservation of mass

In the freeze-drying process water in the form of ice sublimates and diffuses through the dried porous region, but is also bounded in the base material. Due to the water vapor movement from the sublimation front to the orifice of the vial, the contra-movement of inert gas occurs, which also affects the movement of the water vapor. Therefore, the mass conservation law for the inert gas also needs to be accounted for.

The mass conservation laws are written only for the dried region. Therefore, the mass transfer equation for the water vapor can be written in the following form:

$$\epsilon\frac{M_v}{R}\frac{\partial}{\partial t}\left(\frac{p_v}{T}\right) + \vec{\nabla}\cdot\overrightarrow{N_v} = -\rho_{1,p}\frac{\partial C}{\partial t}, \tag{3}$$

where ϵ represents the porosity of the dried material, M_v, the molecular mass of the water, R the ideal gas constant and p_v, the partial pressure of water vapor. The first term on the left hand side represent the accumulation of the water vapor, the second one is convection, while the right hand side represents desorption of bounded water in the base material. The desorption term has a negative sign, which comes from the negative time derivative of the bounded water concentration, making the term positive and the desorption acting as the mass source. The mass conservation for the inert gas is stated in the similar manner, with the exception of desorption:

$$\epsilon\frac{M_i}{R}\frac{\partial}{\partial t}\left(\frac{p_i}{T}\right) + \vec{\nabla}\cdot\overrightarrow{N_i} = 0 \tag{4}$$

where M_i and p_i represent the molecular mass and partial pressure of inert gas, respectively. The first term from the left describes the accumulation of the inert gas and the second one the convection of it. As can be observed, the inert gas and water vapor are treated as the ideal gasses. Since the total pressure and partial pressures of the inert gas and water vapor are in the range of few Pascals, the assumption of ideal gas can be applied.

To describe the mass conservation of both gaseous phases completely, the mass fluxes of the inert gas $\overrightarrow{N_i}$ and the water vapor $\overrightarrow{N_v}$ have to be defined. The gradient model similar to the Darcy law can be used, therefore, the mass fluxes are written in the following form:

$$\overrightarrow{N_v} = -\frac{M_v}{RT}(k_1\vec{\nabla}p_v + k_2p_v(\vec{\nabla}p_v + \vec{\nabla}p_i)), \tag{5}$$

$$\overrightarrow{N_i} = -\frac{M_i}{RT}(k_3\vec{\nabla}p_i + k_4p_i(\vec{\nabla}p_v + \vec{\nabla}p_i)) \tag{6}$$

where k_1 and k_3 are the bulk diffusivity constants and k_2 and k_4 the self diffusivity constants. The bulk constants k_1 and k_3 are very similar and are defined as

$$k_1 = \frac{C_2D^0_{v,i}K_v}{C_2D^0_{v,i} + K_{mx}(p_v + p_i)}, \tag{7}$$

$$k_3 = \frac{C_2D^0_{v,i}K_i}{C_2D^0_{v,i} + K_{mx}(p_v + p_i)} \tag{8}$$

where C_2 represents the constant that depends only upon the structure of the porous region and represents the ratio of bulky diffusivity within the porous medium to the free gas bulk diffusivity, K_v, and K_i are Knudsen diffusivities for the water vapor and inert gas, respectively, K_{mx} is the mean Knudsen diffusivity for binary gas mixture and $D^0_{v,i}$ the free gas mutual diffusivity multiplied by the total pressure:

$$D^0_{v,i} = D_{v,i}(p_v + p_i) \tag{9}$$

Here the $D_{v,i}$ represents the free gas mutual diffusivity for binary gas mixture and $p_v + p_i$ the total pressure in the dried region. The self diffusivity constants k_2 and k_4 are usually taken as equal [17,2,19] and are defined as

$$k_2 = k_4 = \frac{K_vK_i}{C_2D^0_{v,i} + K_{mx}(p_v + p_i)} + \frac{C_{01}}{\mu_{mx}} \tag{10}$$

where C_{01} represents the Darcy flow permeability constant and μ_{mx} the

viscosity of the binary gas mixture in the dried region. The mean Knudsen diffusivity for binary gas mixture can be determined by the equation

$$K_{mx} = \frac{p_v}{p_v + p_i} K_v + \frac{p_i}{p_v + p_i} K_i \tag{11}$$

where the Knudsen diffusivity of inert gas K_i and water vapor K_v are defined as

$$K_i = C_1 \sqrt{\frac{RT}{M_i}} \tag{12}$$

and

$$K_v = C_1 \sqrt{\frac{RT}{M_v}} \tag{13}$$

with C_1 representing the Knudsen flow permeability constant. With the listed mass transfer models the system of equations for the mass transfer of inert gas (4) and water vapor (3) is closed.

3.3. Conditions at the interface

The heat and mass transfer in the freeze-drying process are highly interconnected, as can be seen from Eq. (1), (2), (3) and (4). One of the main features is the ice sublimation process, with water changing the state from solid to vapor, taking place at the sublimation front or the interface dividing the frozen region from the dried one. The mass flux of the water vapor from the sublimation front into the dried region depends on water vapor partial pressure difference between the sublimation front with the saturation pressure $p_v^\star$ and the partial pressure in the surrounding dried porous region. The partial pressure of saturation depends on the interaction of the base material and ice as well as on the temperature, and a dedicated model has to be used. In general the model for saturation pressure can be written in the following form:

$$p_v^\star = B_1 \cdot \exp\left(B_2 - \frac{B_3 dH_v}{T}\right) \tag{14}$$

where B_1, B_2 and B_3 are model constants that depend on the composition of the freeze-drying material. For the case of freeze-drying of the skimmed milk, the model for saturation pressure together with model constants is listed in Table 3.

The desorption process takes place in the already dried region during the drying process on the surface of the porous solid structure. For the mass conservation Eqs. (3) and (4) the rate of desorption has to be determined. In this case the first order kinetics model was used,

$$\frac{\partial C}{\partial t} = k_g (C^\star - C), \tag{15}$$

where k_g represents the mass transfer coefficient and $C^\star$ the equilibrium water concentration, which depends on the partial pressure of the water vapor, the amount of bounded water inside the dried material and temperature. The equilibrium water concentration can be written in the following form:

$$C^\star = A_1 \cdot \exp(A_2 (A_3 - A_4 \cdot (T - T_0))) \tag{16}$$

where A_1, A_2, A_3 and A_4 are the binary mixture constants and T_0 the initial temperature of the frozen material. The model for skimmed-milk is stated in the Table 3.

On the sublimation front dedicated boundary conditions have to be imposed. The first one is the compatibility condition for the heat transfer, stating that the temperature field is continuous. The second condition states that the mass flux of inert gas is equal to zero, $\overrightarrow{N_i} = 0$, and the last one is the equilibrium boundary condition for the heat transfer. The equilibrium boundary condition on the sublimation front takes into consideration the heat flux due to the conduction, the sublimation heat, convection of the water vapor and the movement of the sublimation front, and can be represented as

$$\lambda_{II} \left.\frac{\partial T}{\partial \vec{n}}\right|_{II} + \vec{v}_n \rho_{II} c_{p,II} T = \lambda_{e,I} \left.\frac{\partial T}{\partial \vec{n}}\right|_{I} + \vec{v}_n \rho_{I,p} c_{p,Ip} T - dH_s \overrightarrow{N_{v,n}} - \overrightarrow{N_{v,n}} c_{p,g} T|_I \tag{17}$$

where $\vec{n}$ represents the normal vector of the sublimation front, $\vec{v}_n$ the normal velocity of the sublimation front, $\overrightarrow{N_{v,n}}$ the normal mass flux of the water vapor and $c_{p,Ip}$ the heat capacity of porous material. The first and third term from the left represent the heat flux due to the temperature gradient (Fourier law), the second and fourth term represent the effect of the sublimation front movement, the fifth term is the energy used for the sublimation and the last one the convection of the water vapor. As can be seen the temperature gradient at the interface is discontinuous not only due to the different thermal conductivities but also because of the sublimation process. Of course the normal velocity $\vec{v}_n$ can be linked to the normal mass flux $\overrightarrow{N_{v,n}}$ of water vapor through equation

$$\vec{v}_n = -\frac{\overrightarrow{N_{v,n}}}{\rho_{II} - \rho_{I,p}} \tag{18}$$

with the density difference $(\rho_{II} - \rho_{I,p})$ of the phases.

4. Subdomain boundary element method discretization

The mathematical model of freeze-drying in a vial is non-linear and interconnected, which is impossible to solve analytically, therefore a numerical approach has been used. To transform the governing partial differential equations into their discrete form, the Boundary Element Method (BEM) using the subdomain approach has been used (Ramšak et al. [21,22]). One of the reasons for selecting the BEM as the method of choice is the fact that solution of BEM based discretized equations produces results for the function as well as for the function's derivative with the same order of accuracy.

The problem of heat and mass transfer in a vial under the freeze-drying process in a process device is definitely a three-dimensional problem that depends on the position of the vial in the lyophilization chamber (middle, edge or corner), which affects primarily the heat transfer from the surroundings [8,4]. However, in this paper we decide to investigate the freeze-drying process in only one vial, therefore due to the vial axisymmetrical geometry it is reasonable to treat the problem as axisymmetrical one. The axisymmetrical treatment is also reasonable for the vials that are fully surrounded with other vials [17,2,4].

In the next subsections the description of the BEM numerical scheme for solving the freeze-drying process in a vial under axisymmetric conditions is given, together with the discretization of the governing equations and the resulting numerical solution algorithm.

4.1. Discretization of the poisson equation using BEM

The resulting governing equations can all be cast into the form of the Poisson equation, which is a non-homogeneous elliptic partial differential equation, in general stated as

$$\Delta u(s) + b(s) = 0, \tag{19}$$

where Δ represents the Laplace operator, u stands for the arbitrary field function, b for the source term or the non-homogeneous part and $s = s(x, y, z)$ for the spatial vector. In the case of the freeze-drying governing equations the field function u can represent the temperature or partial pressure, while the non-homogeneous part b represents the accumulation, convection, desorption etc.

As all of the governing equations have the same general properties, derivation of BEM for the general axisymmetrical case is presented first, starting with the integral form of Green's second identity, which in

the case of the Poisson Eq. (19) reads as:

$$c(\xi)u(\xi) = \int_{\Gamma} q(S)u^*(\xi, S)d\Gamma - \int_{\Gamma} u(S)q^*(\xi, S)d\Gamma + \int_{\Omega} b(s)u^*(\xi, s)d\Omega, \tag{20}$$

where $\Omega = \Omega(x, y, z)$ represents the computational domain and $\Gamma = \Gamma(x, y, z)$ the boundary of the computational domain. $S = S(x, y, z)$ is the spatial vector of the boundary, $q = \partial u/\partial n$ normal derivative of the field function, $\xi = \xi(x, y, z)$ is the source point, c the free coefficient that depends on the position of the source point and u^* and $q^* = \partial u^*/\partial n$ are the Green fundamental solution and its normal derivative, respectively. The fundamental solution for the elliptic equation and 3D domain is $u^*(\xi, s) = 1/(4\pi d(\xi, s))$, where $d(\xi, s)$ represents the distance between the source point and arbitrary space point. As can be seen from the integral Eq. (20), we have to evaluate the boundary integrals, as well as the domain one, which can not be avoided in the case of non-homogeneous elliptic equation. In the case of homogeneous elliptic equation the domain integral vanishes and only boundary integrals remain.

Because the problem is treated as axisymmetrical, the cylindrical coordinate system (r, φ, z) is introduced. The elementary volume can be therefore written as $d\Omega = dxdydz = |J|drd\varphi dz$ and the elementary surface $d\Gamma$ as $d\Gamma = |J|d\ell d\varphi$, where $|J|$ is determinant of the Jacobian matrix and is equal to $|J| = r(s)$ for the cylindrical coordinate system, and $d\ell = \sqrt{dr^2 + dz^2}$ represents the elementary distance. The integral Eq. (20) can therefore be rewritten in the form

$$c(\xi)u(\xi) = \int_{\Gamma} q(S)r(S)u^*(\xi, S)d\ell d\varphi - \int_{\Gamma} u(S)r(S)q^*(\xi, S)d\ell d\varphi + \int_{\Omega} b(s)r(s)u^*(\xi, s)drd\varphi dz \tag{21}$$

that can be integrated by the angle φ due to the axisymmetrical treatment, introducing the elementary surface $d\Pi = drdz$ in the following manner:

$$c(\xi)u(\xi) = \int_{\ell}\int_0^{2\pi} q(S)r(S)u^*(\xi, S)d\ell d\varphi - \int_{\ell}\int_0^{2\pi} u(S)r(S)q^*(\xi, S)d\ell d\varphi + \int_{\Pi}\int_0^{2\pi} b(s)r(s)u^*(\xi, s)d\Pi d\varphi, \tag{22}$$

$$c(\xi)u(\xi) = \int_{\ell} q(S)r(S)u^*_{axi}(\xi, S)d\ell - \int_{\ell} u(S)r(S)q^*_{axi}(\xi, S)d\ell + \int_{\Pi} b(s)r(s)u^*_{axi}(\xi, s)d\Pi. \tag{23}$$

With this step we transform the whole 3D computational domain to a quasi 2D domain, represented by the elementary surface $d\Pi$ and the elementary edge $d\ell$. Therefore, we only have to evaluate the curve and surface integrals, which makes it much easier. The axisymmetric fundamental solution can be obtained by integrating the fundamental solution $u^*(\xi, s)$ by the angle φ, as shown above, and can be written as

$$u^*_{axi}(\xi, s) = \frac{K(m)}{\pi(a + b)^{1/2}}, \tag{24}$$

where a, b and m represent the parameters that reflect the distance between the source and arbitrary space point, and $K(m)$ is the complete elliptic integral of the first kind [31]. To be exact the parameters a, b and m read as

$$a = r_\xi^2 + r_s^2 + (z_\xi - z_s)^2, \quad b = 2r_\xi r_s, \quad m = 2b/(a + b). \tag{25}$$

where the source point is defined by the coordinates $\xi = \xi(r_\xi, z_\xi)$ and the arbitrary space point by $s = s(r_s, z_s)$.

The normal derivative of the axisymmetric fundamental solution $q^*_{axi}(\xi, S) = \partial u^*_{axi}(\xi, S)/\partial\vec{n}$, which is also needed in the integral equation (23), is defined by the equation

$$q^*_{axi}(\xi, S) = \frac{1}{\pi(a + b)^{1/2}}\cdot\frac{1}{2r_s}\left(\frac{r_\xi^2 - r_s^2 + (z_\xi - z_s)^2}{a - b}E(m) - K(m)\right)\cdot n_r(S) + \frac{1}{\pi(a + b)^{1/2}}\cdot\frac{z_\xi - z_s}{a - b}E(m)\cdot n_z(S), \tag{26}$$

where $n_r(S)$ and $n_z(S)$ represents the components of the normal vector on the boundary of the computational domain; $\vec{n}(S) = \{n_r(S), n_z(S)\}$, and $E(m)$ is the complete elliptic integral of the second kind [31].

As stated before, the value of the free coefficient $c(\xi)$ depends on the position of the source point ξ and is defined as

$$c(\xi) = 1, \quad \xi \in \Pi, \qquad c(\xi) = \beta/(2\pi), \quad \xi \in \ell. \tag{27}$$

where β represents the outside angle of the edge.

The derived integral Eq. (23) represents the basis of the BEM numerical scheme for solving the axisymmetric elliptic problem that will be used to transform the freeze-drying governing equations into the algebraic form.

For discretization of the domain Π the four node linear cells were used, and for the boundary ℓ, the two node linear elements. The linear elements has been used because of the desired robustness of the numerical model. In order to be able to specify varying material properties in the domain and to directly apply interface conditions at the sublimation front, the subdomain approach was used. For this case, the integral Eq. (23) was written for every cell separately, and the subdomains were assembled into the system of equations by applying the equilibrium and compatibility conditions at the boundaries of subdomains. The used subdomain approach is described in more detail in our previous works [21,22].

For the discretization of the field function $u(s)$ and a non homogeneous part $b(s)$ a continuous linear interpolation function was used, while for the normal derivative of the field function $q(S)$ on the boundary the constant interpolation function was selected. Applying the interpolation functions and evaluating the integrals in the Eq. (23) the algebraic or discrete form of the integral equation is obtained. In order to obtain the full system of equations for a subdomain, the equation is written for the source point ξ positions in every node point of the subdomain. In the final step of obtaining the system of equations for the whole computational domain all equations for subdomains are assembled using the compatibility and equilibrium conditions for adjoin cells, which in the final matrix form reads as

$$[H]\{u\} = [G]\{q\} + [S]\{b\}. \tag{28}$$

where $[H]$, $[G]$ and $[S]$ are the matrices, $\{u\}$ is the vector of discrete values of the field function (in nodes), $\{q\}$ is the vector of discrete values of the field function normal derivative and $\{b\}$ is the vector of discrete values of non-homogeneous part. The system of equations is the discrete form of the elliptic Poison Eq. (19) that can be applied to all governing equations of the freeze-drying problem.

4.2. Heat transfer in the frozen region

To apply the derived discretization scheme to the heat transfer governing equation in the frozen region (2), the equation have to be cast into the non-homogeneous elliptic form as follows,

$$\Delta T + \left(-\frac{\rho_{II}c_{p,II}}{\lambda_{II}}\frac{\partial T}{\partial t}\right) = 0. \tag{29}$$

Now if we compare the Eq. (29) to the Poison Eq. (19), we can observe that the field function $u(r, z)$ represents the temperature $T(r, z)$, while the non-homogenous source part b represents the accumulation term:

$$b = -\frac{1}{a_{II}}\frac{\partial T}{\partial t}, \tag{30}$$

where the thermal diffusivity of the frozen region is $a_{II} = \lambda_{II}/(\rho_{II}c_{p,II})$.

Finally, the time derivative in the non-homogeneous part b is discretized by using the second order asymmetric finite difference scheme,

$$\frac{\partial T}{\partial t} = \frac{3T_t - 4T_{t-1} + T_{t-2}}{2dt}, \tag{31}$$

where dt represents the time step and t, $t-1$ and $t-2$ are successive time indexes. At the start of the time marching the assumption $T_0 = T_{-1}$ is applied in order to use the scheme for all time instants. Including the numerical scheme (31) into the non-homogeneous term (30) and using the connection $u = T_t$ and $q = q_t = \partial T_t/\partial n$, we can write the discrete system of Eq. (28) into the following form

$$[H]\{T_t\} = [G]\{q_t\} - \frac{1}{a_{II}}[S]\left\{\frac{3}{2dt}T_t - \frac{2}{dt}T_{t-1} + \frac{1}{2dt}T_{t-2}\right\}. \tag{32}$$

By deciding to put the part of the accumulation that includes the temperature field at the current time step, to the left hand side or into the system matrix as

$$\left\{[H] + \frac{3}{2a_{II}dt}[S]\right\}\{T_t\} = [G]\{q_t\} + \frac{1}{a_{II}}[S]\left\{\frac{2}{dt}T_{t-1} - \frac{1}{2dt}T_{t-2}\right\}, \tag{33}$$

we obtained the final form of linear system of equations that describes the heat transfer in the frozen region in every time step, which can be solved in one iteration loop. The system (33) represents the discrete form of heat transfer equation in the frozen region using BEM.

4.3. Heat transfer in the dried region

For numerical approximation of the energy conservation equation in the dried region (1) a similar approach is used as in the case of the frozen region. However, the equation in the presented form does not include the Laplace operator, which is the basis for the derivation of the elliptic discretization scheme by BEM. This is because of the non-homogeneous thermal conductivity, which is temperature dependent and therefore also space dependent. In order to obtain the suitable form of the equation, the diffusion term is rewritten in the following form

$$\Delta T + \left(\frac{1}{\lambda_{e,I}}\vec{\nabla}\lambda_{e,I}\vec{\nabla}T + \frac{dH_v\rho_{l,p}}{\lambda_{e,I}}\frac{\partial C}{\partial t} - \frac{1}{a_{e,I}}\frac{\partial T}{\partial t} - \frac{1}{\lambda_{e,I}}\vec{\nabla}\cdot[(\overrightarrow{N_v} + \overrightarrow{N_i})c_{p,g}T]\right) = 0, \tag{34}$$

where $a_{e,I}$ represents the effective thermal diffusivity of the dried region, $a_{e,I} = \lambda_{e,I}/(\rho_{e,I}c_{pe,I})$. The field function $u(r, z)$ for this governing equation is the temperature $T(r, z)$, while the source part b includes all the non-homogeneous term like non-homogeneous diffusion, desorption, accumulation and convection:

$$b = \frac{1}{\lambda_{e,I}}\vec{\nabla}\lambda_{e,I}\vec{\nabla}T + \frac{dH_v\rho_{l,p}}{\lambda_{e,I}}\frac{\partial C}{\partial t} - \frac{1}{a_{e,I}}\frac{\partial T}{\partial t} - \frac{1}{\lambda_{e,I}}\vec{\nabla}\cdot[(\overrightarrow{N_v} + \overrightarrow{N_i})c_{p,g}T]. \tag{35}$$

Because some of the terms inside the source b like $\vec{\nabla}T$ would be very difficult to obtain directly, explicit computation based on the computed values of the function from the previous non-linear solution iteration is used. With the introduction of the following notation

$$P = \vec{\nabla}\lambda_{e,I}\vec{\nabla}T,\ D = \partial C/\partial t, \tag{36}$$

$$K = -\vec{\nabla}\cdot[(\overrightarrow{N_v} + \overrightarrow{N_i})c_{p,g}T],$$

implementation of the time approximation scheme (31) and by setting $u = T_t$ and $q = q_t = \partial T_t/\partial n$, we can rewrite the discrete elliptical numerical scheme (28) into

$$\left([H] + \frac{3}{2a_{e,I}dt}[S]\right)\{T_t\} = [G]\{q_t\} + \frac{1}{\lambda_{e,I}}[S]\{P_t\} + \frac{dH_v\rho_{l,p}}{\lambda_{e,I}}[S]\{D_t\} + \frac{2}{a_{e,I}dt}[S]\{T_{t-1}\} - \frac{1}{2a_{e,I}dt}[S]\{T_{t-2}\} + \frac{1}{\lambda_{e,I}}[S]\{K_t\}, \tag{37}$$

where the part of accumulation has been shifted to the left hand side to improve the numerical stability of the computations. To solve the heat transfer equation in its discrete form (37), we had to include the non-linear iteration loop inside the time step, because of the right hand side evaluation of the temperature gradient $\vec{\nabla}T_t$ from the known values of the previous non-linear iteration loop.

4.4. Inert gas mass transfer

As in the case, described in Section 4.3, the governing equation for the inert gas (4) has to be recast into form containing the Laplace operator on the function. By applying the gradient model of the inert gas mass flux (6) into the inert gas mass conservation equation the following form of the equation is obtained,

$$\epsilon\frac{\partial}{\partial t}\left(\frac{p_i}{T}\right) - \vec{\nabla}\cdot\left[\frac{k_3}{T}\vec{\nabla}p_i + \frac{k_4}{T}p_i(\vec{\nabla}p_v + \vec{\nabla}p_i)\right] = 0. \tag{38}$$

By considering the molecular mass M_i and ideal gas constant R as constants and after some derivations the governing Eq. (38) is transformed into the elliptic form, which does include the Laplace operator of partial pressure of the inert gas

$$\left(\frac{k_3}{T} + \frac{k_4}{T}p_i\right)\Delta p_i + \left[\left(\vec{\nabla}\left(\frac{k_3}{T}\right) + \frac{k_4}{T}(\vec{\nabla}p_v + \vec{\nabla}p_i)\right)\cdot\vec{\nabla}p_i - \epsilon\frac{\partial}{\partial t}\left(\frac{p_i}{T}\right) + \left(\vec{\nabla}\left(\frac{k_4}{T}\right)\cdot(\vec{\nabla}p_v + \vec{\nabla}p_i) + \frac{k_4}{T}\Delta p_v\right)p_i\right] = 0. \tag{39}$$

Finally, the non-homogenous part b has to be determined. By introducing the variables

$$\omega_i = \frac{k_3}{T} + \frac{k_4}{T}p_i,\ \vec{\psi_i} = \vec{\nabla}\left(\frac{k_3}{T}\right) + \frac{k_4}{T}(\vec{\nabla}p_v + \vec{\nabla}p_i), \tag{40}$$

$$\sigma_i = \vec{\nabla}\left(\frac{k_4}{T}\right)\cdot(\vec{\nabla}p_v + \vec{\nabla}p_i) + \frac{k_4}{T}\Delta p_v$$

the non-homogenous part is rewritten in the following form

$$b = \frac{\vec{\psi_i}}{\omega_i}\cdot\vec{\nabla}p_i + \frac{\sigma_i}{\omega_i}p_i - \frac{\epsilon}{\omega_i}\frac{\partial}{\partial t}\left(\frac{p_i}{T}\right). \tag{41}$$

Evaluating the gradients of partial pressure, temperature, constant k_3 and k_4, as well as the Laplace of liquid partial pressure Δp_i is performed in the non-linear iteration loop within a single time step. The arbitrary field function $u(r, z)$ in this case represents the partial pressure of inert gas $p_i(r, z)$. The time derivative inside the source part b has been discretized with the numerical scheme (31), as

$$\frac{\partial}{\partial t}\left(\frac{p_i}{T}\right) = \frac{3p_{i,t}}{2T_t dt} - \frac{2p_{i,t-1}}{T_{t-1}dt} + \frac{p_{i,t-2}}{2T_{t-2}dt}. \tag{42}$$

Implementing the Eq. (41), time derivative discretization (42) and by considering $u = p_{i,t}$ and $q = \partial p_{i,t}/\partial n$ into the BEM numerical scheme (28), the discrete form of the mass conservation equation for the inert gas is obtained

$$\left([H] + \frac{3\epsilon}{2\omega_i T_t dt}[S] - \frac{\sigma_i}{\omega_i}[S]\right)\{p_{i,t}\} = [G]\{q_t\} + \frac{1}{\omega_i}[S]\{R_i\} + \\ + \frac{2\epsilon}{\omega_i T_{t-1} dt}[S]\{p_{i,t-1}\} - \frac{\epsilon}{2\omega_i T_{t-2} dt}[S]\{p_{i,t-2}\}, \tag{43}$$

where $R_i = \vec{\psi}_i \cdot \vec{\nabla} p_i$. As before, a part of the accumulation term $(\sigma_i \cdot p_i)/\omega_i$ is included into the system matrix. Due to the non-linear nature, the equation is solved in an iterative manner inside each time step.

4.5. Water vapor mass transfer

To solve the mass transfer of the water vapor in the dried region by using the derived BEM scheme, we encounter the same problems as in the inert gas case. Identical transformation procedure is therefore applied, starting by applying the gradient model of mass flux (5) into the governing Eq. (3), followed by the derivation which leads to the following form of the governing equation

$$\epsilon \frac{\partial}{\partial t}\left(\frac{p_v}{T}\right) = \omega_v \Delta p_v + \vec{\psi}_v \cdot \vec{\nabla} p_v + \sigma_v p_v - \rho_{1,p} \frac{R}{M_v} \frac{\partial C}{\partial t}, \tag{44}$$

with the new variables defined

$$\omega_v = \frac{k_1}{T} + \frac{k_2}{T} p_v, \quad \vec{\psi}_v = \vec{\nabla}\left(\frac{k_1}{T}\right) + \frac{k_2}{T}(\vec{\nabla} p_v + \vec{\nabla} p_i), \\ \sigma_v = \vec{\nabla}\left(\frac{k_2}{T}\right) \cdot (\vec{\nabla} p_v + \vec{\nabla} p_i) + \frac{k_2}{T} \Delta p_i. \tag{45}$$

Now the Eq. (44) can be rewritten in the elliptic form (19) as

$$\Delta p_v + \left[\frac{\vec{\psi}_v}{\omega_v} \cdot \vec{\nabla} p_v + \frac{\sigma_v}{\omega_v} p_v - \frac{\epsilon}{\omega_v} \frac{\partial}{\partial t}\left(\frac{p_v}{T}\right) - \frac{\rho_{1,p}}{\omega_v} \frac{R}{M_v} \frac{\partial C}{\partial t}\right] = 0, \tag{46}$$

where the field function $u(r, z)$ represents the partial pressure of the water vapor $p_v(r, z)$ and the non-homogeneous source part b the accumulation part, desorption and all other effects from the gradient mass flux model:

$$b = \frac{\vec{\psi}_v}{\omega_v} \cdot \vec{\nabla} p_v + \frac{\sigma_v}{\omega_v} p_v - \frac{\epsilon}{\omega_v} \frac{\partial}{\partial t}\left(\frac{p_v}{T}\right) - \frac{\rho_{1,p}}{\omega_v} \frac{R}{M_v} \frac{\partial C}{\partial t}. \tag{47}$$

The computation of the sources is done in the non-linear iteration loop inside a time step, where the gradients of partial pressure, the Laplace of the inert gas partial pressure and other terms like desorption rate are iteratively evaluated. As before, the time derivative approximation (42) is also implemented.

Finally, the following matrix form of the discretized equation is obtained

$$\left([H] + \frac{3\epsilon}{2\omega_v T_t dt}[S] - \frac{\sigma_v}{\omega_v}[S]\right)\{p_{v,t}\} = [G]\{q_t\} + \frac{1}{\omega_v}[S]\{R_v\} + \\ + \frac{2\epsilon}{\omega_v T_{t-1} dt}[S]\{p_{v,t-1}\} - \frac{\epsilon}{2\omega_v T_{t-2} dt}[S]\{p_{v,t-2}\} \\ - \frac{\rho_{1,p} R}{\omega_v M_v}[S]\{D\}, \tag{48}$$

where $R_v = \vec{\psi}_v \cdot \vec{\nabla} p_v$ and $D = \partial C/\partial t$ stands for the desorption rate.

4.6. Desorption of bounded water

The desorption ob the bounded water inside the dried region can be modeled as a first-order kinetic problem (15), which does not include the Laplace operator and therefore cannot be discretized using the derived BEM numerical scheme. To determine the desorption rate and the concentration of the bounded water in each time step we decided to implement the time derivative form (31), resulting in

$$C_t = \frac{2k_g dt C^* - 4C_{t-1} + C_{t-2}}{2k_g dt - 3}, \tag{49}$$

where $C^* = C^*(T)$ is determined by the empirical model (16). The bounded water concentration can be explicitly computed in every time step and every mesh node by knowing the concentration history and the temperature field for the calculation of the equilibrium concentration C^*, which finally allows the computation of the desorption rate

$$\frac{\partial C}{\partial t} = -\frac{3C_t}{2dt} + \frac{2C_{t-1}}{dt} - \frac{C_{t-2}}{2dt}. \tag{50}$$

4.7. Sublimation front

The interface boundary between the frozen and the dried region is represented by the sublimation front, where sublimation process occurs and dictates the speed of freeze-drying process. Therefore the sublimation process on the sublimation front had to be treated very carefully. The sublimation process or conservation of heat fluxes at the interface is described with boundary condition (17), which connects the two regions together.

The decision has been made to couple the heat transfer equations for the dried and the frozen region through the boundary condition (17), which has been rewritten in the scalar form by including the definition of normal velocity (18) and normal derivative of the temperature field $q_{II} = \partial T/\partial n|_{II}$ and $q_I = \partial T/\partial n|_I$ as

$$\lambda_{II} q_{II} = -\lambda_{e,I} q_I + N_{v,n}\left(\frac{T}{\rho_{II} - \rho_{I,p}}(\rho_{II} c_{p,II} - \rho_{I,p} c_{p,Ip}) - dH_s - c_{p,g} T\right) \tag{51}$$

where $N_{v,n}$ represent the value of the normal mass flux of the water vapor from the sublimation front; $N_{v,n} = \overrightarrow{N_{v,n}} \cdot \vec{n}$. With this approach, the boundary condition at the sublimation front depends only on $N_{v,n}$ variable, which is determined by the mass flux gradient model (5) from the known partial pressure of inert gas and water vapor, obtained from the mass transfer equations. The equilibrium boundary condition (51), which couples the two heat transfer equations together, is updated through the non-linear iteration loop inside the time step in the form of

$$q_{II} = -\frac{\lambda_{e,I}}{\lambda_{II}} q_I + \frac{1}{\lambda_{e,I}} Q_m, \tag{52}$$

where Q_m represents the convection and sublimation effects on the sublimation front as

$$Q_m = N_{v,n}\left(\frac{T}{\rho_{II} - \rho_{I,p}}(\rho_{II} c_{p,II} - \rho_{I,p} c_{p,Ip}) - dH_s - c_{p,g} T\right). \tag{53}$$

The discrete versions of governing equations are strongly coupled and had to be solved within each time step by implementing an internal non-linear iteration loop.

4.8. Moving mesh at the sublimation front

At the end of each time step, when all field functions (temperature, partial pressure of water vapor etc.) converged inside the non-linear iteration loop, the movement of the sublimation front can be determined. The movement can be determined explicitly by the Eq. (18), using the known mass flux of water vapor at the interface, which is calculated from the known constants and partial pressures by the model (5). In order to control the changes in the mesh topology as the sublimation front progresses, the Eq. (18) has been rewritten to the following form

$$\vec{v} = \dot{\vec{r}} = -\frac{\overrightarrow{N_v}}{\rho_{II} - \rho_{I,p}}, \tag{54}$$

where the definition of the velocity $\vec{v} = \dot{\vec{r}}$, with $\vec{r}$ representing the

spatial vector of node, was used. The · represents a time derivative. The governing Eq. (54) for sublimation front movement has been used in the component form as

$$\dot{r} = -\frac{N_{v,r}}{\rho_{II} - \rho_{I,p}}, \quad \dot{z} = -\frac{N_{v,z}}{\rho_{II} - \rho_{I,p}}. \tag{55}$$

There is no need for a higher order numerical scheme to determine the new position, therefore the most simple first-order finite difference numerical scheme was implemented, giving the discrete equations of movement in the radial and z-direction as

$$r_t = r_{t-1} - \frac{N_{v,r}dt}{\rho_{II} - \rho_{I,p}}, \quad z_t = z_{t-1} - \frac{N_{v,z}dt}{\rho_{II} - \rho_{I,p}}. \tag{56}$$

Because of implementing the structured mesh generation algorithm within the computational code, the very slow movement of the sublimation front allowed to fix the computational mesh in the radial direction ($r_t = r_{t-1}$) and to permit only the node movement in the z-direction. After the node movement and recomputation of the mesh, the interpolation and extrapolation of the results from the previous to the new computational mesh was performed in order to start the calculation in the next time step.

4.9. Computational algorithm

The complex nonlinear system of equations, described in the previous subsections, has to be solved in an iterative computational procedure. In order to get a better view of the solution process, the algorithm is presented in the following paragraph form:

1. Start of the numerical simulation.
2. Defining the position of the sublimation front.
3. Numerical mesh generation.
4. Determination of initial conditions for temperature, partial pressures and liquid concentration.
5. Start of the time step of the primary drying stage:
   - Calculation of matrices $[H]$, $[G]$ and $[S]$.
   - Start of the non-linear iteration loop:
     - Calculation of the liquid desorption - Eqs. (49) and (50).
     - Coupled calculation of the heat transfer for both regions - Eqs. (33) and (37), using the equilibrium conditions at the sublimation front - Eq. (52).
     - Calculation of mass transfer coefficients k_1, k_3 and $k_2 = k_4$ - Eqs. (7), (8) and (10).
     - Calculation of mass transfer for the inert gas - Eq. (43).
     - Calculation of mass transfer for the water vapor - Eq. (48).
     - Correction of coefficients k_1, k_3 and $k_2 = k_4$ using new values of partial pressures p_v and p_i.
     - Calculation of mass fluxes: $\overrightarrow{N_v}$ and $\overrightarrow{N_i}$ - Eqs. (5) and (6).
   - End of the non-linear iteration loop.
   - Calculation of the new sublimation front position - Eq. (56).
   - Generation of the new computational mesh.
   - Interpolation of results (variables) to the new computational mesh.
6. End of the time step computation within the primary drying stage.
7. Check if the sublimation front reached the bottom of the vial, if not the next time step in the primary drying is computed (point 5). In the case of reaching the bottom the computation continues with the secondary drying stage.
8. Computational mesh generation (only porous domain).
9. Computation of matrices $[H]$, $[G]$ and $[S]$, done only once, as the geometry for the secondary drying stage remains constant.
10. Interpolation and extrapolation of the results from the primary drying stage to the porous domain for setting the initial conditions of the secondary drying stage.
11. Start of the time stepping in the secondary drying stage:
    1. Start of the non-linear iteration loop:
       - Calculation of the liquid desorption - Eqs. (49) and (50).
       - Heat transfer calculation in the porous domain - Eq. (37).
       - Calculation of mass transfer coefficients k_1, k_3 and $k_2 = k_4$ - Eqs. (7), (8) and (10).
       - Calculation of mass transfer for the inert gas - Eq. (43).
       - Calculation of mass transfer for the water vapor - Eq. (48).
       - Correction of coefficients k_1, k_3 and $k_2 = k_4$.
       - Calculation of mass fluxes: $\overrightarrow{N_v}$ and $\overrightarrow{N_i}$ - (5) and (6).
    2. End of non-linear iteration loop.
12. End of the time step computation within the secondary drying stage.
13. Check on the bounded liquid concentration C. If the concentration is $C > 0.05$ continue the computation with the next time step - return to the point 11.
14. End of the numerical simulation.

5. Computational example: freeze-drying of skimmed milk in vial

Numerical simulation of the freeze-drying in a vial can be a very demanding task to perform, as there are many unknown model parameters or material properties under freeze drying conditions. Also, a limited data on suitability of the used models like the gradient model of mass fluxes in porous domains or correctness of the liquid desorption model for different solid-liquid mixtures bring further uncertainties, complemented by the lack of data on exact boundary conditions on the domain boundaries. The freeze-drying process in a vial is of course strongly connected to the heat and mass transfer in the whole lyophilization chamber and to be able to successfully model the freeze-drying process one should consider the whole system. Limiting the computation to a single vial and comparing the solution to an experimental one can therefore be very demanding task to do.

However, the proposed numerical approach has to be tested and for the reasons stated above, we could not have tested it considering real experimental data. The developed numerical scheme was tested on the reference example of the freeze-drying of the skimmed milk, taken from Mascarenhas et al. [17]. In the following, details on the computational domain, initial and boundary conditions and material data used are given, followed by the validation of the simulation results, comparison and discussion.

5.1. Computational domain data

The computational domain considers only the material inside the vial (the frozen and dried porous regions) omitting the geometry of the vial, as also reported by Mascarenhas et al. [17]. Considering the computational domain used by Mascarenhas et al. [17] we can represent the domain by the cylinder of radius $R = 1$ mm and the height of $H = 3$ mm. Because of the axisymmetrical treatment, the computational domain is represented with one half of the axial cross-section, as can be depicted from the Fig. 2, where the used computational mesh is also shown.

A dedicated computational code was developed for the process of discretisation of the computational domain, as it had to be implicitly incorporated into numerical movement of the sublimation front during the simulation. It is linked to the changes of the size of the two subdomains and with that also the size and the number of the mesh elements. For the domain discretization two different criterion have been chosen, the first is the minimal number of elements in the z direction, which is 5, and the second one is the characteristic length of the element dl. Based on these two criteria the number of elements or nodes in the z and r direction has been determined. The regular computational mesh was recomputed every time step, because of the moving sublimation front, by using the same number of nodes in each

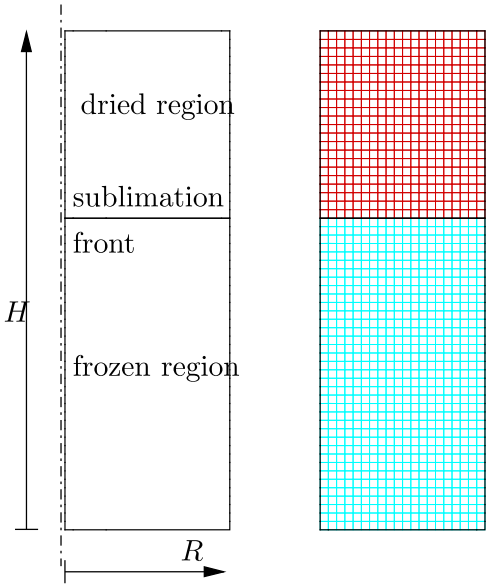

Fig. 2. Geometry and computational mesh for freeze drying of skim milk.

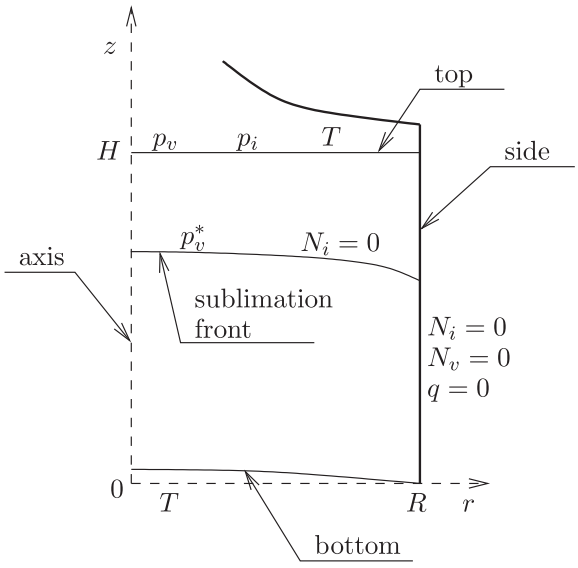

Fig. 3. Axisymmetric representation of the vial with boundary conditions.

direction. If the mesh elements became too distorted (too large or too small in the z direction) the new number of elements or nodes in each sub-domain was selected, based on the described criteria, and the computational mesh was recomputed. Fig. 2 shows the implemented equidistant structured computational mesh in each sub-domain for one particular time step.

5.2. Initial and boundary conditions

The initial condition, boundary conditions, material properties and model constants needed for numerical simulation of the freeze-drying of the skimmed milk were taken from Mascarenhas et al. [17]. The material properties, used mathematical models and constants are gathered in the Table 3. The initial condition for the temperature was taken to be $T_0 = 241.8$ K, while the partial pressure of the inert gas was $p_{i,0} = 4$ Pa and the partial pressure of the water vapor $p_{v,0} = 5.2668$ Pa. The initial total pressure in the dried region is then $p_0 = p_{i,0} + p_{v,0} = 9.2668$ Pa, which is equal to the pressure in the lyophilization chamber. The equilibrium concentration of adsorbed water in the dried region for the given temperature, calculated from the model for $C^\star$ in Table 3, was set to $C_0 = 0.2283$ kg/kg.

Boundary conditions for all three variables, temperature, partial pressure of inert gas and of water vapor, depicted in Fig. 3, were set separately for the primary and the secondary drying stage, and are reported in Tables 1 and 2.

At the top side the Dirichlet boundary conditions for all three variables are prescribed, while at the bottom side only the Dirichlet condition for the temperature is set, since the mass conservation equations for the water content is not solved in the frozen region. At the sublimation front, only the boundary condition for the mass transfer has to be prescribed, while the boundary condition for the heat conservation is included in the system of equations, governing the movement of the sublimation front. The boundary conditions for the partial pressures at the sublimation front are derived from the fact, that the mass flux of inert gas at the front is zero, i.e. $\overrightarrow{N_i} = 0$, and from the fact that the partial pressure of the water vapor is identical to the saturated partial pressure, i.e. $p_v^\star$, which is calculated by the model stated in Table 3. Also the adsorbed water concentration at the interface is set as the equilibrium condition calculated from the model for $C^\star$ in Table 3 and given interface temperature. The boundary condition on the symmetry axis is the zero gradient condition of Neumann type. The zero gradient conditions for the partial pressures come from the fact that there is no mass flow of inert gas or water vapor through the glass ($\overrightarrow{N_i} = 0$ and $\overrightarrow{N_v} = 0$). On the side of the vial the heat flux q was set to zero, allowing comparison of results to the result of Mascarenhas et al. [17], obtained by using one dimensional approach.

The difference between the primary and the secondary drying stage is mainly in the change of boundary conditions and computational domain, which in the secondary stage consists of porous domain only. For the secondary drying stage there is no interface or sublimation front, therefore the computational mesh is set constant during this part of computation. At the bottom part of the domain only the temperature is elevated during the secondary stage. Because there is no sublimation front anymore the boundary conditions for the partial pressures at the bottom are set as zero mass flux.

The freeze-drying simulation starts with the two regions existence, as at the top there exist already a small dried region with the height of 2% of the total height of the material in the vial. The error because of this simplification is estimated to be very small, as the dried region represents only a small fraction of the frozen material. The primary drying stage is assumed to be completed when the sublimation front reaches the bottom 2% of the total height. In the computed test case this means that the simulation starts with the sublimation height of

Table 1
Prescribed boundary conditions for the primary drying stage.

Boundary	Boundary condition
top	$T = 303.15$ K, $p_v = 5.2668$ Pa, $p_i = 4$ Pa
bottom	$T = 263.15$ K
sublimation front	$\partial p_i/\partial n = 0$, $p_v = p_v^\star$
axis	$\partial T/\partial n = 0$, $\partial p_i/\partial n = 0$, $\partial p_v/\partial n = 0$
side	$\partial T/\partial n = 0$, $\partial p_i/\partial n = 0$, $\partial p_v/\partial n = 0$

Table 2
Prescribed boundary conditions for the secondary drying stage.

Boundary	Boundary condition
top	$T = 303.15$ K, $p_v = 5.2668$ Pa, $p_i = 4$ Pa
bottom	$T = 303.15$ K $\partial p_i/\partial n = 0$, $\partial p_v/\partial n = 0$
axis	$\partial T/\partial n = 0$, $\partial p_i/\partial n = 0$, $\partial p_v/\partial n = 0$
side	$\partial T/\partial n = 0$, $\partial p_i/\partial n = 0$, $\partial p_v/\partial n = 0$

Table 3
Value and models of different variables for skimmed milk.

Variable	Value or model
C_{01}	$7.219 \cdot 10^{-15}$ m^2
C_1	$3.85583 \cdot 10^{-4}$ m
C_2	0.4428
C^*	$0.01\exp(2.3(1.36 - 0.036(T - T_0))$
k_g	$11.08 \cdot 10^{-5}$ s^{-1}
$p_v^\star$	133.32 Pa$\cdot\exp(23.9936 - \frac{2.19\Delta H_v}{T})$
dH_v	2791.2 kJ/kg
dH_s	2791.2 kJ/kg
k_2, k_4	0
M_i	29 kg/kmol
M_v	18 kg/kmol
R	8314 J/kmol K
μ_{mx}	$[18.4858(T^{1.5}/(T + 650))]$ kg/ms
$D^0_{v,i}$	$8.729 \cdot 10^{-7}(T_0 + T_{int})^{2.334}$ kg/ms^3
K_v	$1.429 \cdot 10^{-4}\sqrt{T_0 + T_{int}}$ m^2/s
K_i	$K_v \cdot \sqrt{M_v/M_i}$ m^2/s
$c_{p,g}$	1674.7 J/kgK
$c_{p,lp}$	2595 J/kgK
$c_{p,II}$	1967.8 J/kgK
$c_{pe,I}$	2595 J/kgK
$\lambda_{e,I}$	$680[12.98 \cdot 10^{-8}(p_i + p_v) + 39.806 \cdot 10^{-6})]W/mK$
λ_{II}	2.1 W/mK
ϵ	0.706
$\rho_{I,p}$	145 kg/m^3
ρ_{II}	1058 kg/m^3
$\rho_{e,I}$	327.6 kg/m^3 $= 0.2\rho_{II} + 0.8\rho_{I,p}$

2.94 mm and the primary drying stage ends at the sublimation height of 0.06 mm, when it switches to the secondary drying stage. The simulation stops when the bounded water concentration falls below the predefined level, in our case 5% or $C = 0.05$ kg/kg.

5.3. Code validation and mesh independence study

The used Subdomain BEM code has been successfully validated in many of our papers. For example the stream function vorticity equation solver was introduced in the paper [21]. Recently the code was tested for the solution of the large scale general diffusion problems consisting of multimillion mesh nodes [22]. The conjugate heat transfer benchmark problem was computed using the present code in [32].

To validate the results of primary and secondary drying stage, an analysis of how the space and time domain discretization impacts the results, especially the drying time. The analysis of space domain discretization effect on results is presented in Table 4.

Reducing the characteristic length of the mesh element (*dl*) one can observe that the time for primary and secondary drying stage converge. For the secondary drying stage results converge much faster then for the primary, where the effect of the moving sublimation front and mesh deformation is very pronounced. However, the change between the two

Table 4
Primary and secondary drying time dependency on element length *dl*. Time step value used is 1 s *Delta* is drying time change between two sequential results.

	Primary drying			Secondary drying up to 5%		
dl [mm]	Time [s]	*Delta* [%]	CPU [h]	Time [h]	*Delta* [%]	CPU [h]
0.2	905	1.1	0.03	3.88	0.3	0.02
0.1	895	0.7	0.16	3.87	0.0	0.05
0.05	889	0.5	0.93	3.87	0.0	0.25
0.025	885		6.81	3.87		1.28

Table 5
Primary and secondary drying time dependency on time step *dt* value. Element length *dl* is 0.1 mm. *Delta* is drying time change between two sequential results.

	Primary drying			Secondary drying up to 5%		
dt [s]	Time [s]	*Delta* [%]	CPU [h]	Time [h]	*Delta* [%]	CPU [s]
1000				4.16	6.1	27
100				3.92	1.3	62
10	880	−1.7	0.04	3.87	0.0	138
1	895	0.4	0.26	3.87		978
0.1	891	0.2	1.30			
0.01	889		7.04			

adjoin cases is minimal and in the range of 1% or less. For the final computations the element size of $dl = 0.05$ mm was chosen, which produced accurate results with moderate computational times.

5.4. Time step independence study

As the freeze drying process is very slow process with process times in range of several hours or even more, a time marching should be done by using as large time steps as possible, but without loosing too much accuracy. The analysis of time step size on the accuracy of the results is shown in the Table 5, where for the space discretization a constant element size of 0.1 mm has been used.

The time step value was varied between 0.01 s and 1000 s, where smaller time steps have been chosen only for the primary drying stage and the larger ones for the secondary drying stage. Using small time step value is appropriate for the primary drying stage, because of the greater system non-linearity, while it is inappropriate for the secondary stage due to resulting very long computational times. From the results it can be concluded that for the primary drying stage, the reasonable time step value can be between 1 s and 0.1 s, as smaller time steps drastically increase the computational time. For the secondary drying stage it is reasonable to take as large time step as possible to reduce the computational time. In order to limit the numerical error due to time stepping procedure, the values between 100 s and 10 s are acceptable. Based on the error analysis, for the final computations the value of $dt_{pr} = 0.1$ s for the time step for the primary drying stage and $dt_{sec} = 10$ s for the secondary time step were selected.

5.5. Results and discussion

Table 6 summarizes the drying times for the primary and secondary drying stage obtained using the derived Subdomain BEM algorithm along with comparison to results of Mascarenhas [17] and Millman [16]. It can be concluded that the results are in good agreement and that the difference with the other authors is in the range of 9% for the primary drying stage and 2% for the secondary drying stage.

Although the results for primary drying stage show a higher error it can be observed from the Fig. 4 that the dynamics of the sublimation front height h_s is accurate in the average sense, but with a faster sublimation at the beginning and a slower sublimation towards the end of the primary drying stage.

The Fig. 5 presents the temperature variation in time at a certain height for the primary drying stage. The sudden temperature jump is the indication of the sublimation front passing a certain point or

Table 6
Primary and secondary drying time comparison with references.

Drying time [min]	Primary	Secondary
BEM	14.77	232.20
Mascarenhas [17]	13.77	228.92
Millman [16]	13.47	231.82

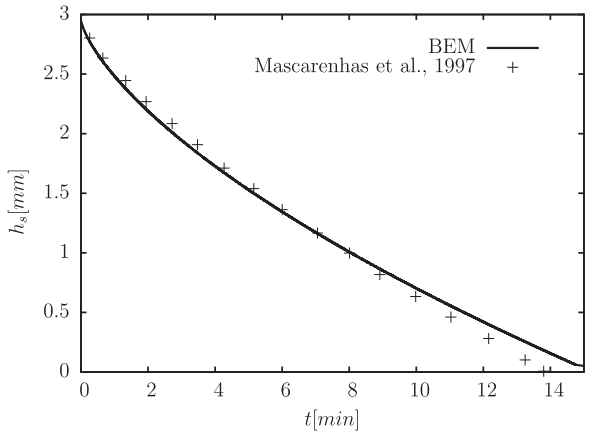

Fig. 4. Sublimation front height dynamics.

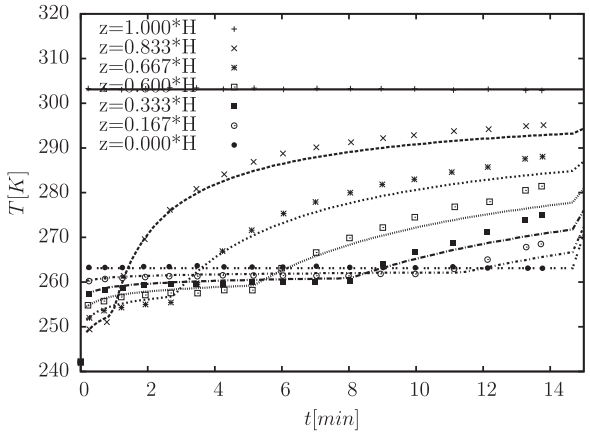

Fig. 5. Temperature at different height versus time during primary drying. BEM results are plotted with lines and results of Mascarenhas [17] with points.

height. After that such as point is positioned in the dried region, where the desorption process of bounded water is taking place. The Fig. 5 also shows the comparison with Mascarenhas [17], where a good agreement is observed together with minor deviations in the dried region. For a better imagination the contour of temperature field at different time is shown in Fig. 6, where also the position of the sublimation front can be seen.

Fig. 7 presents temporal dynamics of bounded water concentration for the primary drying stage at predetermined points, which exhibit good agreement with results of Mascarenhas [17]. The temporal

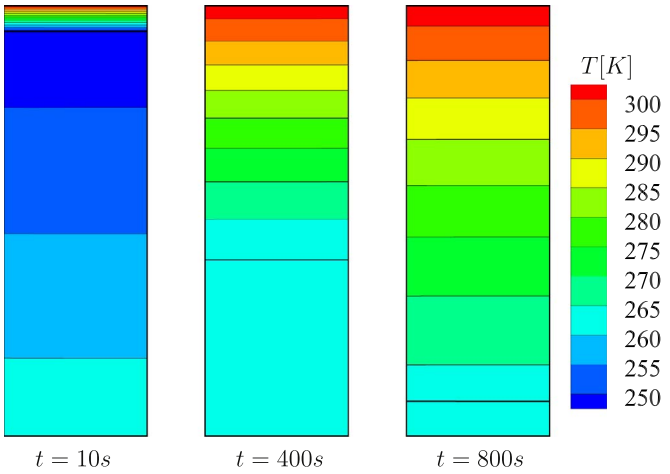

Fig. 6. Temperature contour at different times for primary drying stage.

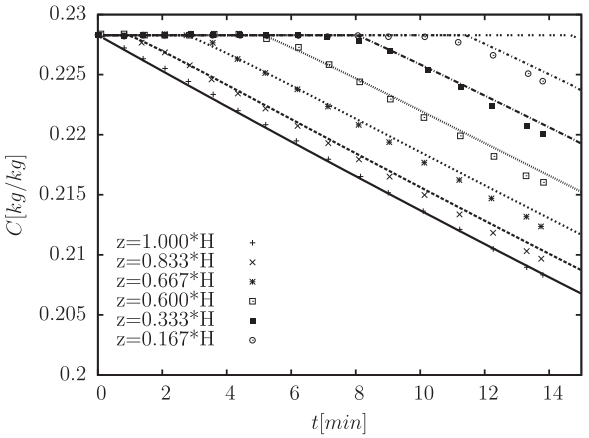

Fig. 7. Adsorbed water concentration at different heights versus time during primary drying. BEM results are plotted with lines and results of Mascarenhas [17] with points.

change of water concentration is very linear, which corresponds with the used first-order kinetic model (15). Fig. 8 shows the contour of bounded water concentration during the primary drying stage at different times for better visualization.

Fig. 9 shows the change of bounded water concentration through time in the secondary drying stage but only for the highest and lowest point. The reason is in more clear presentation of the results and clear

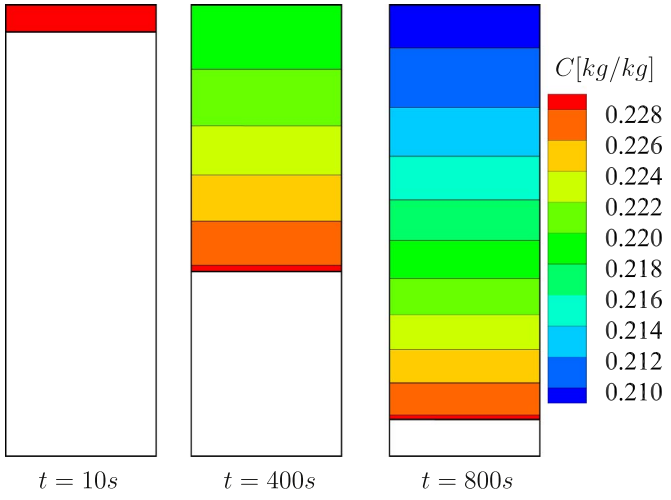

Fig. 8. Bounded water concentration contour at different times for primary drying stage.

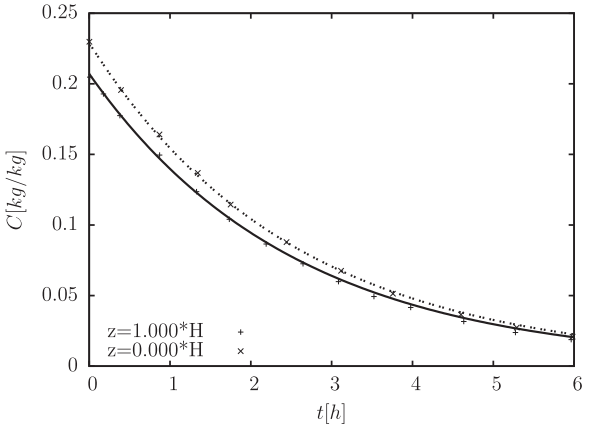

Fig. 9. Adsorbed water concentration at top and bottom versus time during secondary drying stage. BEM results are plotted with lines and results of Mascarenhas [17] with points.

comparison with Mascarenhas [17]. Otherwise, the bounded water concentration is linearly distributed in the dried region. The results show nearly a perfect match with Mascarenhas and an exponential behavior through time till the desired dryness level.

The differences of obtained results in comparison with results of Mascarenhas [17] can be most likely attributed to the facts that in the presented approach the mass flux constants are corrected inside the non-linear iteration loop, the energy conservation equations are solved in both regions simultaneously, and heat diffusion in the dried region is treated as non-homogeneous, while Mascharenhas used the homogeneous diffusion approach.

6. Conclusions

The complex mathematical model of coupled heat and mass transfer in porous and non-porous domains is solved with the Subdomain BEM approach, where the freeze-drying process in a vial is treated as axisymmetrical one. The proposed new numerical model builds on the elliptic fundamental solution, treating the governing equations in elliptic Poison's form. The time derivative was approximated with the second order FD scheme. To implement the derived numerical scheme for computation of the mass conservation governing equations, these had to be restated due to the lack of Laplace operator. Including the mass flux models into the mass conservation equations yields the appropriate elliptic form, which can be discretised by the proposed BEM approach. The sublimation process is incorporated into the interface heat flux boundary condition, for which the energy conservation equation has been simultaneously solved in the frozen and dried regions. The interface condition was reformulated in order to contain only the normal mass flux of water vapor as the unknown variable that is updated through the iteration process. Because of the highly interconnected system of governing equations, the non-linear iteration loop has been introduced in each time step to update the variables and to evaluate some unknown terms in discretised equations. Because of the moving sublimation front the simulation of the primary drying stage is computationally the most expensive part, as the computational mesh has to be regenerated in every time step, leading to computation of new boundary and domain integrals.

The proposed numerical scheme has been tested on the example of freeze-drying of skimmed milk in a vial. The results with other authors show a good agreement which indicates that the proposed numerical approach is appropriate, accurate and by using an appropriate numerical mesh and time step values also reasonably fast.

Although the problem has been approximated as axisymmetrical one, it still provides a detailed insight into local as well as global conditions of mass and heat transfer in the vial. In case of vials as solution containers, the derived model can also be implemented in a more complex numerical simulation of mass and heat transfer in the whole dryer containing several hundred or even thousand vials. Development of a dedicated numerical model for freeze drying is the first step in developing a CFD based freeze-drying model, where full solution of the fluid flow with heat and mass transfer in the drying chamber will be coupled to solution of BEM based submodels for drying inside the vials, followed by comparison with experimental determination of temperature kinetics inside the vials. In this way, the validated coupled CFD-BEM numerical model will be a powerful computational tool for determination of global as well as local efficiencies of the freeze-drying process.

References

[1] Liapis A, Bruttini R. Freeze-drying of pharmaceutical crystalline and amorphous solutes in vials: dynamic multi-dimensional models of the primary and secondary drying stages and qualitative features of the moving interface. Dry Technol 1995;13(1–2):43–72.

[2] Sheehan P, Liapis AI. Modeling of the primary and secondary drying stages of the freeze drying of pharmaceutical products in vials: numerical results obtained from the solution of a dynamic and spatially multi-dimensional lyophilization model for different operational policies. Biotechnol Bioeng 1998;60(6):712–28.

[3] Cornu O, Banse X, Docquier P-L, Luyckx S, Delloye C. Effect of freeze-drying and gamma irradiation on the mechanical properties of human cancellous bone. J Orthop Res 2000;18(3):426–31.

[4] Gan KH, Bruttini R, Crosser OK, Liapis AI. Heating policies during the primary and secondary drying stages of the lyophilization process in vials: effects of the arrangement of vials in clusters of square and hexagonal arrays on trays. Dry Technol 2004;22(7):1539–75.

[5] Pikal M, Roy M, Shah S. Mass and heat transfer in vial freeze-drying of pharmaceuticals: role of the vial. J Pharm Sci 1984;73(9):1224–37.

[6] Liapis A, Bruttini R. Exergy analysis of freeze drying of pharmaceuticals in vials on trays. Int J Heat Mass Transf 2008;51(15):3854–68.

[7] Brülls M, Rasmuson A. Heat transfer in vial lyophilization. Int J Pharm 2002;246(1):1–16.

[8] Gan KH, Bruttini R, Crosser OK, Liapis AI. Freeze-drying of pharmaceuticals in vials on trays: effects of drying chamber wall temperature and tray side on lyophilization performance. Int J Heat Mass Transf 2005;48(9):1675–87.

[9] Sadikoglu H, Liapis A, Crosser O. Optimal control of the primary and secondary drying stages of bulk solution freeze drying in trays. Dry Technol 1998;16(3–5):399–431.

[10] Daraoui N, Dufour P, Hammouri H, Hottot A. Model predictive control during the primary drying stage of lyophilisation. Control Eng Pract 2010;18(5):483–94.

[11] Alexeenko AA, Ganguly A, Nail SL. Computational analysis of fluid dynamics in pharmaceutical freeze-drying. J Pharm Sci 2009;98(9):3483–94.

[12] Petitti M, Barresi AA, Marchisio DL. Cfd modelling of condensers for freeze-drying processes. Sadhana 2013;38(6):1219–39.

[13] Massey W, Sunderland J. Heat and mass transfer in semi-porous channels with application to freeze-drying. Int J Heat Mass Transf 1972;15(3):493–502.

[14] Litchfield R, Liapis AI. An adsorption-sublimation model for a freeze dryer. Chem Eng Sci 1979;34(9):1085–90.

[15] Sadikoglu H, Liapis A. Mathematical modelling of the primary and secondary drying stages of bulk solution freeze-drying in trays: parameter estimation and model discrimination by comparison of theoretical results with experimental data. Dry Technol 1997;15(3–4):791–810.

[16] Millman M, Liapis A, Marchello J. An analysis of the lyophilization process using a sorption-sublimation model and various operational policies. AIChE J 1985;31(10):1594–604.

[17] Mascarenhas W, Akay H, Pikal M. A computational model for finite element analysis of the freeze-drying process. Comput Methods Appl Mech Eng 1997;148(1):105–24.

[18] Song C, Nam J. A numerical study on freeze drying characteristics of cylindrical products with and without container. Int J Transp Phenom 2005;7(3):241.

[19] Song C, Nam J, Kim C-J, Ro S. A finite volume analysis of vacuum freeze drying processes of skim milk solution in trays and vials. Dry Technol 2002;20(2):283–305.

[20] Nam JH, Song CS. An efficient calculation of multidimensional freeze-drying problems using fixed grid method. Dry Technol 2005;23(12):2491–511.

[21] Ramšak M, Škerget L, Hriberšek M, Žunič Z. A multidomain boundary element method for unsteady laminar flow using stream function - vorticity equations. Eng Anal Bound Elem 2005;29:1–14.

[22] Ramšak M, Škerget L. A highly efficient multidomain bem for multimillion subdomains. Eng Anal Bound Elem 2014;43:76–85.

[23] Ravnik J, Škerget L, Žunič Z. Velocity-vorticity formulation for 3d natural convection in an inclined enclosure by bem. Int J Heat Mass Transf 2008;51(17):4517–27.

[24] Ravnik J, Hriberšek M, Lupše J. Lagrangian particle tracking in velocity-vorticity resolved viscous flows by subdomain bem. J Appl Fluid Mech 2016;9(3):1533–49.

[25] Škerget L, Tadeu A, Ravnik J. Bem simulation model for coupled heat, moisture and air transport through a multilayered porous wall. WIT Trans Model Simul 2015;61:249–60.

[26] Iljaž J, Škerget L. Blood perfusion estimation in heterogeneous tissue using bem based algorithm. Eng Anal Bound Elem 2014;39:75–87.

[27] Partridge PW, Wrobel LC. A coupled dual reciprocity bem/genetic algorithm for identification of blood perfusion parameters. Int J Numer Methods Heat Fluid Flow 2009;19(1):25–38.

[28] Šarler B, Kuhn G. Dual reciprocity boundary element method for convective-diffusive solid-liquid phase change problems, part 1. formulation. Eng Anal Bound Elem 1998;21(1):53–63.

[29] Šarler B, Kuhnb G. Dual reciprocity boundary element method for convective-diffusive solid-liquid phase change problems, part 2. numerical examples. Eng Anal Bound Elem 1998;21(1):65–79.

[30] Šarler B, Mavko B, Kuhn G. A survey of the attempts for the solution of solid-liquid phase change problems by the boundary element method. in: Computational methods for free and moving boundary problems in heat and fluid flow, London; New York: Computational Mechanics Publisher: Elsevier Applied Science, 1993.

[31] Wrobel LC. The Boundary Element Method, Applications in Thermo-Fluids and Acoustics, 1. John Wiley & Sons; 2002.

[32] Ramšak M. Conjugate heat transfer of backward-facing step flow: a benchmark problem revisited. Int J Heat Mass Transf 2015;84:791–9.